




MUSEnet: High Temporal-Frequency Estimation of Landslide Deformation Field Through Joint InSAR and Hydrological Observations Using Deep Learning

Aoqing Guo , Qian Sun , Jun Hu , *Senior Member, IEEE*, Wanji Zheng , Rong Gui , and Yana Yu 

Abstract—The Three Gorges hydropower station in China creates a large reservoir by diverting water from the Yangtze River, increasing the risk of geological disasters, especially massive landslides along the reservoir shoreline. To mitigate these risks, improving geological monitoring and early warning systems is crucial. Interferometric Synthetic Aperture Radar (InSAR) is widely used to monitor reservoir bank landslides. However, its potential in early warning systems is limited due to temporal resolution constraints, preventing timely warnings. To address this, we propose integrating daily hydrological data (precipitation and water level observations) with historical InSAR deformation sequences using our deep learning-based multivariate united state estimation network, “MUSEnet.” This approach generates customized daily landslide deformation products for high-risk areas, greatly enhancing early warning capabilities by providing timely and accurate information on landslide occurrence and magnitude. We validated our method using 161 Sentinel-1 A images of the Xinpu landslide in the Three Gorges Reservoir area. Through statistical analysis, we identified different degrees of influence from rainfall and reservoir water level on the deformation of the Xinpu landslide at various locations. Additionally, we observed distinct lag times between deformation and corresponding rainfall and reservoir water level events. By utilizing deep learning, our method estimates nonlinear states by considering hysteresis and intelligently accounts for the impact of rainfall and reservoir water level, resulting in more accurate estimations compared to traditional models.

Index Terms—Deep learning, InSAR, landslide, prediction.

Manuscript received 19 September 2023; revised 1 November 2023; accepted 20 November 2023. Date of publication 1 December 2023; date of current version 15 December 2023. This work was supported in part by the National Natural Science Foundation of China under Grant 42030112, in part by the Nature Science Foundation of Hunan Province under Grant 2022JJ30031, in part by the science and technology innovation Program of Hunan Province under Grant 2022RC3042, in part by the fundamental research funds for the central universities of Central South University under Grant 2022ZZTS0104, and in part by the Hunan Provincial Innovation Foundation For Postgraduate under Grant CX20220192. (*Corresponding author: Qian Sun.*)

Aoqing Guo, Wanji Zheng, and Yana Yu are with the School of Geosciences and Info Physics, Central South University, Changsha 410083, China (e-mail: guoaoqing@csu.edu.cn; zhengwanji@csu.edu.cn; yuyanamm@csu.edu.cn).

Qian Sun is with the College of Geographic Science, Hunan Normal University, Changsha 410081, China (e-mail: sandra@hunnu.edu.cn).

Jun Hu and Rong Gui are with the Key Laboratory of Metallogenic Prediction of Nonferrous Metals and Geological Environment Monitoring, Ministry of Education, and the Hunan Geological Disaster Monitoring, Early Warning and Emergency Rescue Engineering Technology Research Center, and the School of Geosciences and Info Physics, Central South University, Changsha 410083, China (e-mail: csuhujun@csu.edu.cn; ronggui@csu.edu.cn).

Digital Object Identifier 10.1109/JSTARS.2023.3338449

I. INTRODUCTION

CHINA’S Three Gorges Hydropower Station, one of the world’s largest, has created an immense artificial reservoir by redirecting water from the Yangtze River. This reservoir plays a vital role in regulating water flow and facilitating stable water transport. However, it also introduces an increased risk of geological disasters, particularly numerous landslides along the reservoir banks. As the water levels rise and fall, creep phenomena can occur in the rock and soil of the reservoir slope [1]. These sudden and destructive landslides can rapidly slide into the reservoir, generating massive waves within a matter of seconds. Consequently, they pose a significant threat to human lives and property [2], [3].

The use of historical surface deformation evolution has proven to be valuable in predicting the risk of landslide collapse in advance [4], [5], [6], [7]. The Global Navigation Satellite System (GNSS) is a technology capable of monitoring real-time deformation in areas prone to landslides. However, GNSS monitoring stations located in deformation areas are susceptible to damage, and the available GNSS observations often have limited spatial coverage, which hinders obtaining a comprehensive view of landslide deformation on a global scale [8]. In contrast to GNSS, Interferometric Synthetic Aperture Radar (InSAR) can provide high-resolution spatial information on landslide deformation [9], [10] and is not affected by weather conditions or daylight. However, due to the revisit period of SAR satellites, InSAR can only monitor landslides at a low frequency, lacking the ability to provide daily updates on the development of deformation areas [11]. For instance, between August 9 and August 18, 2016, a sudden small shallow landslide with a displacement of 62 mm occurred on the Xinhua slope of the Dagangshan reservoir area in Sichuan, China, following heavy rainfall [12]. Unfortunately, the Sentinel-1 satellite, which is the most commonly used SAR data source for deformation monitoring, updates its data every 12 days and was unable to capture this deformation signal in a timely manner [13].

Reservoir bank landslides are influenced by a combination of geological, geomorphological, and hydrological factors. They exhibit specific spatio-temporal patterns in terms of their shape, movement characteristics, and overall development trend. These patterns offer crucial prior environmental information for analyzing InSAR time series deformation [14]. Numerous studies have shown that bank landslides are highly responsive to factors

such as precipitation and fluctuations in reservoir water levels. The regulation of pore pressure resulting from these factors leads to the occurrence of slow-moving landslides that exhibit annual seasonal cycles [15], [16]. By considering the causal relationship between landslide deformations and hydrologic observations, it is possible to enhance the accuracy and feasibility of early warning systems for landslides on reservoir banks [17], [18]. Furthermore, integrating landslide deformations with hydrologic observations can effectively minimize the time gap in detecting deformations using InSAR. This approach enables the estimation of landslide states at a high temporal-frequency (HTF) resolution, providing more timely and accurate information for monitoring and response purposes.

Indeed, methods for estimating the deformation state of landslides (EDSL) can be broadly categorized into model-driven and data-driven approaches. Model-driven methods aim to establish quantitative relationship models between deformation and factors such as rainfall or reservoir water levels, utilizing techniques like Kalman filtering (KF) [19]. These methods estimate the optimal deformation state by fitting the model to the observed data. However, studies have shown that the relationship between rainfall and landslide behavior is not straightforward. The cumulative effect of long-term rainfall can trigger landslide movement [20], and there may not be a one-to-one mapping between rainfall and deformation. Furthermore, this relationship is often nonlinear and exhibits a time lag [21]. For example, research on the Krini landslide in Greece found a lag time of 13.5 days between maximum rainfall and landslide displacement [22], while landslides in southern Oregon, USA, showed a lag time of 1-2 months during the rainy season [23]. Therefore, it is crucial to determine the specific lag time for each landslide monitoring point to achieve optimal EDSL using model-driven methods. In addition, certain sections of a landslide may be more susceptible to variations in reservoir water levels, whereas others may be primarily impacted by rainfall. Consequently, if the model is unable to assign appropriate weights to these influencing factors in a dynamic manner, it could result in inaccurate estimation of deformation.

On the other hand, data-driven methods directly analyze historical deformation sequences to predict future deformations. Techniques such as long short-term memory (LSTM) [24] and support vector machine (SVM) [25] are commonly used for univariate deformation estimation. However, these methods can only provide results consistent with the frequency of the input historical deformation data [26]. The temporal resolution of deformation fields obtained from existing methods, which rely on SAR data with a revisit period of typically 11 to 24 days, may lack the necessary level of detail. To overcome these limitations, it is necessary to develop a deep learning algorithm that combines the advantages of both model-driven and data-driven methods. This hybrid approach would leverage the quantifiable relationship models while incorporating the flexibility and precision of deep learning techniques. By doing so, it would be possible to achieve high-precision estimation of EDSL on a daily basis.

Hereby, we have acquired a total of 161 Sentinel-1 A images covering Xinpu, China, from 1st August 2016 to 19th

February 2022. In order to obtain historical deformation data, we employed the independent component analysis (ICA)-assisted time coherent point (TCP) InSAR processing algorithm, which provided us with temporal deformation at a resolution of 12 days. For hydrological observations, we utilized freely available rainfall data in conjunction with water level data from a funded database, these observations were incorporated into our analysis to capture the influence of hydrological factors on landslide deformation. Our objective is to achieve HTF estimation of deformation in the area by integrating the processed deformation data with hydrological observations. To accomplish this, we propose a deep learning network-MUSEnet, which adapts its parameters based on InSAR-derived historical deformations and the associated influencing factors in various scenarios. Unlike the linear state estimation algorithm represented by KF [19], [27], MUSEnet does not require a predetermined functional relationship between hydrological observations and landslide deformation. Instead, it acquires this relationship through adaptive neuron parameter computations. By leveraging this relationship, MUSEnet enables HTF state estimation of landslide deformation.

II. METHODOLOGY

A. Algorithm Flow

First, to obtain the time series deformation field of a landslide, we employ ICA-assisted TCP-InSAR technology. TCP-InSAR technology mitigates the interference from incoherent signals by screening for temporal coherence, thereby preventing unwrapping errors associated with phase ambiguities. Additionally, ICA technology allows for noise separation within the mixed signal, facilitating extraction of the ground deformation signal and enhancing the quality and reliability of InSAR data. This approach enables measurement of line-of-sight (LOS) distances, which are subsequently geocoded (see Fig. 1).

Second, to generate an estimated dataset, we combined daily rainfall data, reservoir level height measurements, InSAR-derived low-frequency deformation values, and their respective timestamps. The details regarding the number and duration of these data are explicitly provided in Section III-C.

Third, based on the time-varying frequency characteristics of HTF hydrological observations from InSAR and low temporal-frequency deformation data, we constructed a deep learning network. The dataset was divided into a training dataset and a test dataset. The training dataset was used to train the deep learning network, which consisted of a time-delay feature extraction module and a state estimation module. The network is detailed in Section II-B.

The test dataset was fed into the estimation model to estimate the HTF deformation. The accuracy of EDSL was evaluated using four evaluation metrics: Root mean square error (RMSE), mean absolute error (MAE), mean absolute percentage error (MAPE), and Pearson correlation coefficient (PCC). Based on the evaluation results, the optimal response parameters of the model were adjusted. The algorithm flowchart, as shown in Fig. 1, presents a step-by-step depiction of the algorithm's application process.

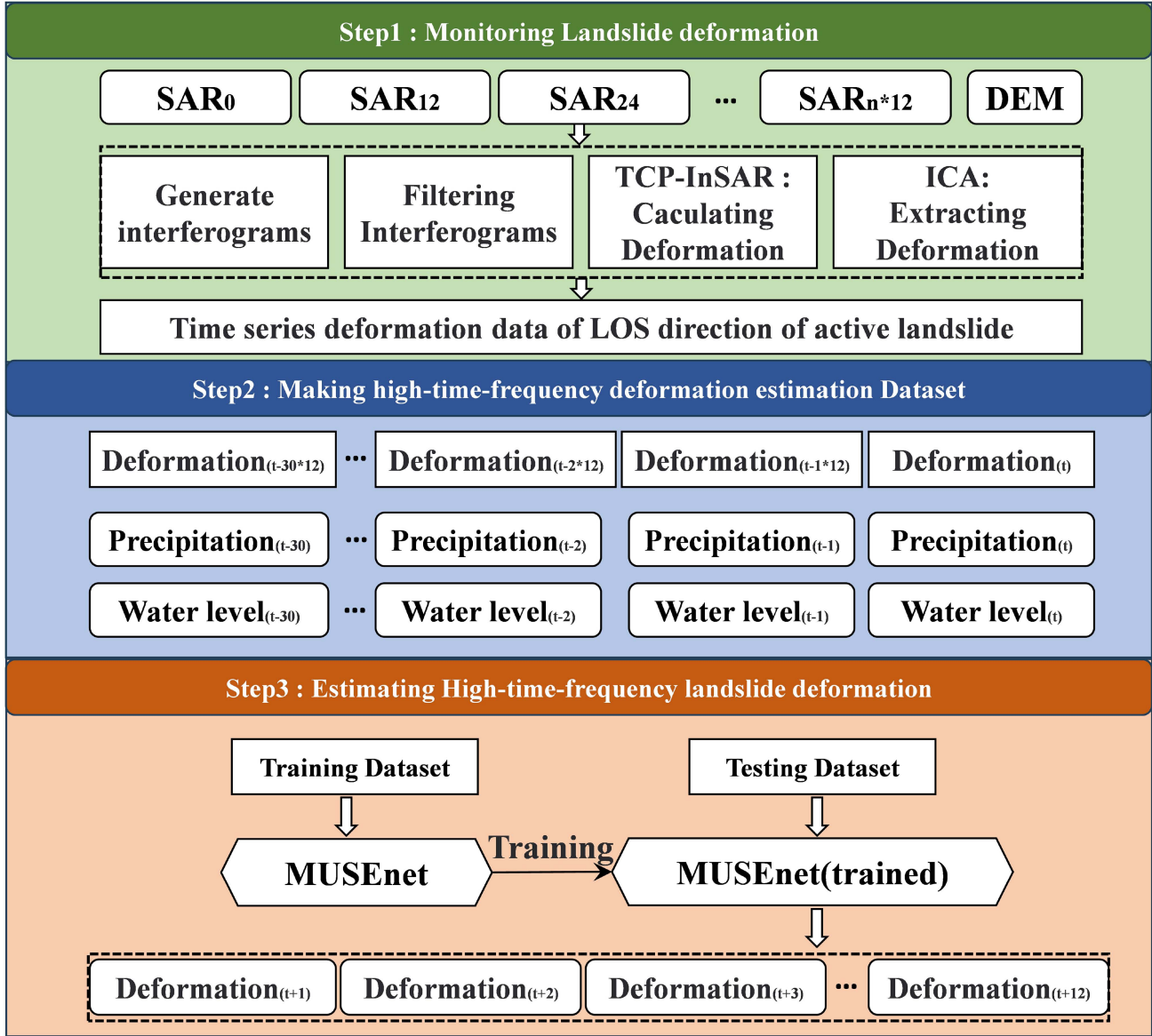


Fig. 1. Flowchart of the method.

B. MUSEnet

Among the various factors that affect landslide deformation, there are rainfall, reservoir water level, the location and slope of the landslide, as well as the geological properties of the soil and the physical properties of surface vegetation. However, due to the difficulty in obtaining all the data related to these factors, in this article, we classify the influencing factors of landslide deformation into fixed factors and nonfixed factors based on their stability over time. Fixed factors refer to the deformation that remains unchanged throughout the year or factors that result in similar deformation patterns occurring every year for the landslide, such as slope gradient, slope direction, location, soil properties, and surface vegetation. Nonfixed factors refer to those whose occurrence or degree of change cannot be determined and their influence on landslide deformation is difficult to ascertain, such as rainfall and reservoir water level. Since

the impact of fixed factors on landslide deformation remains constant every year, we can predict future deformation patterns by utilizing historical deformation patterns at specific points. However, the impact of nonfixed factors needs to be updated daily and adjusted in real time. Reservoir landslide deformation is effectively characterized by considering both historical deformation and hydrological factors. Historical deformation provides insights into the systematic and regular behavior of a slope under specific conditions. On the other hand, hydrological factors, including rainfall and reservoir water level, have an immediate impact on reservoir landslide deformation while also exhibiting a lag effect. The lag effect is influenced by various geological conditions such as slope lithology, shape, and location. Additionally, the intensity and frequency of variations in reservoir water level and rainfall further contribute to the overall deformation pattern [28]. To enhance the MUSEnet network’s capability in coordinating historical deformation and

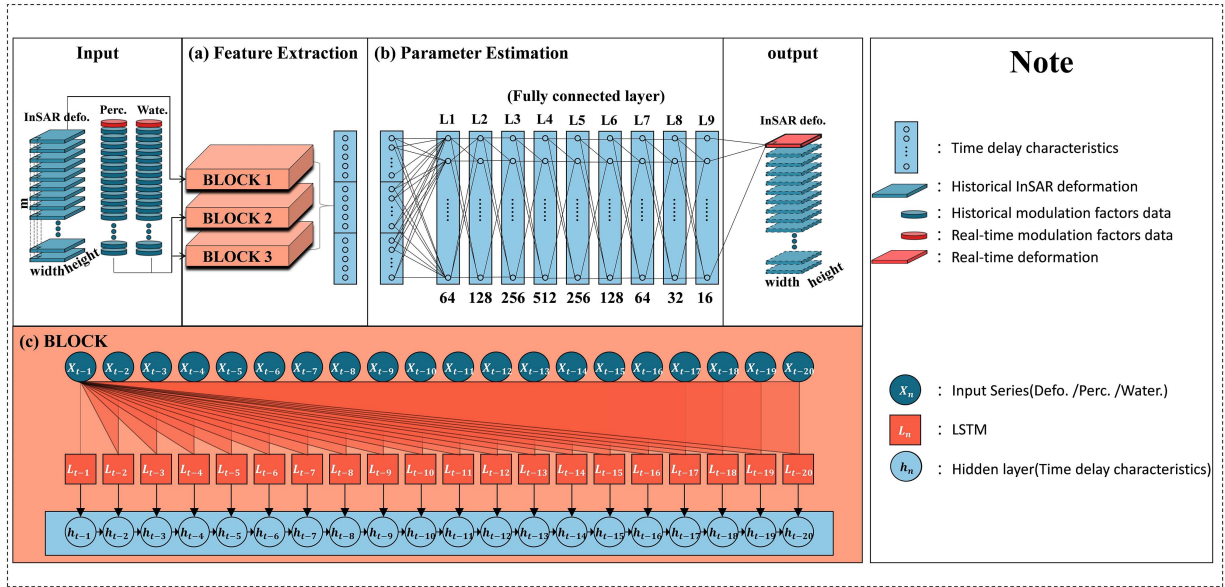


Fig. 2. MUSEnet architecture consists of (a) the feature extraction part, which comprises several blocks; (b) the parameter estimation part, which comprises nine fully connected layers that compute the relationship; and (c) the internal structure of a BLOCK, which is constructed using LSTM and used to extract time-lag information. The input to the BLOCK is the dataset X, while the output is the feature information.

hydrological factors, two modules, namely time-lag feature extraction and state parameter estimation, are integrated into the network. The time-lag feature extraction module facilitates the collaboration of the three types of data, enabling them to extract time series features without interference [29]. In addition, this module calculates time-lag features, which capture the temporal relationships between historical deformation and hydrological factors. By incorporating these features, the network gains a deeper understanding of the interplay between the two types of data, resulting in more accurate estimations and analysis. Obtaining the time-lag features serves the purpose of identifying the lagging or advancement of deformation in relation to rainfall or reservoir water levels. This information is crucial to ensure that when new rainfall or reservoir water levels are acquired, the corresponding deformation value can be obtained without any delay or advancement. The state parameter estimation module follows the time-lag feature extraction module and aims to learn and simulate the function of the time-lag features derived from historical deformation and hydrological factors. This integration allows for the fusion of InSAR and hydrological data, enabling an accurate estimation of EDSL (see Fig. 2).

1) *Feature Extraction*: The feature extraction module in MUSEnet aims to adaptively extract the temporal lag features of landslide deformation, including both systematic deformation features and lag features influenced by various factors. The long short term memory (LSTM) algorithm [30] has been proven as an efficient tool for preserving valuable information in time series data [24]. Therefore, in our new approach MUSEnet, a feature extraction module based on LSTM has been developed with the purpose of capturing lagged deformations and lagged features related to rainfall and reservoir water level. These features exhibit dynamic changes over time, providing a solid foundation for subsequent HTF deformation estimation.

We organized historical deformation and hydrological factors, including rainfall and reservoir water level, along with their temporal information, into datasets. These datasets were fed into BLOCK1, BLOCK2, and BLOCK3 in order to extract time series features. To illustrate, if precipitation is the only influencing factor, then only BLOCK1 and BLOCK2 are utilized. BLOCK1 processes InSAR time series data to extract deformation time delay features, while BLOCK2 processes rainfall data to extract rainfall time delay features. The time range for the historical deformation data is $[t-1, \dots, t-n]$, where n is the length of time that continues to affect subsequent deformation. For rainfall data, the time range is $[t-1, \dots, t-m]$, where m is the lag time of landslide deformation caused by rainfall. It is not possible to accurately estimate m and n artificially, but setting them to a larger value does not have an impact on prediction accuracy.

The sequence was fed into the LSTM in reverse order, and three gates and a self-updating unit in the LSTM start working. The forgetting gate g^e controls the weight of the current information; the external input gate g^e adds new information; the output gate q^e controls the information that needs to be output; the state inside the cell goes through a self-renewing unit s^e . The mathematical foundations of feature extraction networks can be represented by

$$f^e = \sigma \left(b^f + \sum_j U_j^f x_j^e + \sum_j W_j^f h_j^{e-1} \right) \quad (1)$$

$$g^e = \sigma \left(b^g + \sum_j U_j^g x_j^e + \sum_j W_j^g h_j^{e-1} \right) \quad (2)$$

$$q^e = \sigma \left(b^o + \sum_j U_j^o x_j^e + \sum_j W_j^o h_j^{e-1} \right) \quad (3)$$

$$s^e = f^e s^{e-1} + g^e \sigma \left(b + \sum_j U_j x_j^e + \sum_j W_j h_j^{e-1} \right) \quad (4)$$

$$h^e = \tanh(s^e) q^e \quad (5)$$

where e is the sequence number of the feature; j is the sequence number of the input data, from $t-1$ to e , t is the sequence number of the output data; b , U , and W are the bias, input weight and cycle weight in LSTM cells, respectively; $\sigma(*)$ and $\tanh(*)$ are sigmoid function, which are used as the activation function of neural networks to map variables between 0 and 1 or -1 and 1.

For BLOCK1, as e goes through $[t-1, \dots, t-n]$, h^e also exhibits varying deformation time delay characteristics. Similarly, for BLOCK2, as e goes through $[t-1, \dots, t-m]$, h^e has different precipitation time delay characteristics, which can be expressed as (6). In the feature extraction part, we obtained the time delay characteristics of deformation and rainfall/reservoir water level $[H_{\text{def}} H_{\text{pre}}]$

$$\begin{bmatrix} H_{\text{def}} \\ H_{\text{pre}} \end{bmatrix} = \begin{bmatrix} F_1(X(E_1); \theta_1) \\ F_2(X(E_2); \theta_2) \end{bmatrix}. \quad (6)$$

Here, $H_{\text{def}} = [H_{\text{def}}^{e_1}, H_{\text{def}}^{e_2}, \dots, H_{\text{def}}^{e_m}]$ represents the deformation time delay characteristics vector and $H_{\text{pre}} = [H_{\text{pre}}^{e_1}, H_{\text{pre}}^{e_2}, \dots, H_{\text{pre}}^{e_n}]$ represents the precipitation time delay characteristics vector. F_1 and F_2 denote the functional relationships between the input data and their features, respectively, while θ_1 and θ_2 represent the parameters of the function obtained after training. X refers to the input data. $E_1 = [t-1], [t-1, t-2], \dots, [t-1, t-2, \dots, t-m]$ and $E_2 = [t-1], [t-1, t-2], \dots, [t-1, t-2, \dots, t-n]$ represent the time series of information involved in the features.

2) *Parameter Estimation*: After feature extraction, it is necessary to estimate the nonlinear correlations between deformation delay characteristics, rainfall/reservoir water level delay characteristics, and the state that need to be updated. The L-layer deep neural networks (DNN) network calculates the weight and bias of neurons based on the relationship between features and state values, with the rectified linear unit (ReLU) activation function used to modify the linear element and simplify the calculation process. The mathematical foundations of parameter estimation networks can be represented by (7) and (8). Subsequently, the weight of each feature is iteratively updated by calculating the loss value between truth- and calculated values, and the training process is expressed in (9). We can then obtain the optimal relationship between the deformation delay characteristics, rainfall/reservoir water level time delay characteristics, and the state to be updated

$$\begin{cases} H_0 = \begin{bmatrix} H_{\text{def}} \\ H_{\text{pre}} \end{bmatrix} \\ H_{i+1} = \text{ReLU}(W_i H_i + b_i), i = 0, 1, \dots, L-2 \\ H_L = W_{L-1} H_{L-1} + b_{L-1}. \end{cases} \quad (7)$$

Abbreviated as

$$H_L = G(H_0, \theta_3) = G\{F(X(E); \theta)\}. \quad (8)$$

In (7) and (8), b , W are bias and input weight in DNN cells, respectively; H_L is the predicted final state

$$\hat{\theta} = \text{argmin} \left\| \widetilde{H}_L - G\{F(X(E); \theta)\} \right\|^2. \quad (9)$$

In (9), $X(E)$ represents the training dataset, θ represents the initial parameter, and F and G denote the relations for feature extraction and parameter estimation, respectively. $\hat{\theta}$ represents the training parameter.

C. Experimental Details

For this task, our hyperparameter settings are as follows: One layer of LSTM is applied to the feature extraction, and ten layers of DNN are applied to the parameter estimation with the different dimensions (i.e., [input_dim, 64], [64, 128], [128, 256], [256, 512], [512, 256], [256, 128], [128, 64], [64, 32], [32, 16], [16, 1]). The m square error (MSE) loss function is used to score the prediction effect, and the Adam optimization algorithm is used to iteratively update the parameters of MUSEnet based on the training data, with a learning rate of $1e-4$.

D. Comparison Methods

In the comparative experiment of this study, three estimation methods are used to evaluate and compare their performance. The first approach is KF, this model-driven estimation method is widely used for state estimation in various fields. It utilizes a recursive algorithm to estimate the state of a system based on dynamic models and noisy measurements [31]. The second method combines KF with autoregressive integrated moving average (KF-ARIMA) model. This method uses the ARIMA model to capture behavior that changes over time. Before applying KF for deformation estimation correction, ARIMA is used for univariate deformation prediction, which improves the subsequent estimation accuracy. The third method is KF-LSTM, which combines KF with LSTM, a type of recurrent neural network. The LSTM component helps capture long-term dependencies and temporal patterns in the data. Before applying KF for deformation estimation correction, LSTM is used for univariate deformation prediction, enhancing estimation performance. These three methods were compared in experimental tests to evaluate their effectiveness relative to the new method and to compare their performance.

III. DATA SOURCES AND ANALYSIS OF DEFORMATION CAUSES

A. Study Area

The study area is situated in Xinpu Village, Anping Township, within the Three Gorges Reservoir Area in China [see Fig. 3(b)]. The Xinpu landslide, influenced by multistage activities [32], can be divided into three sections: DaPing (DP), ShangErTai (SET), and XiaErTai (XET) slopes, from top to bottom. Previous studies have indicated a strong correlation between rainfall and water level fluctuations with the deformation of the Xinpu landslide. These hydrological factors play a significant role in driving and influencing the movement and behavior of the landslide in this area [33], [34], [35].

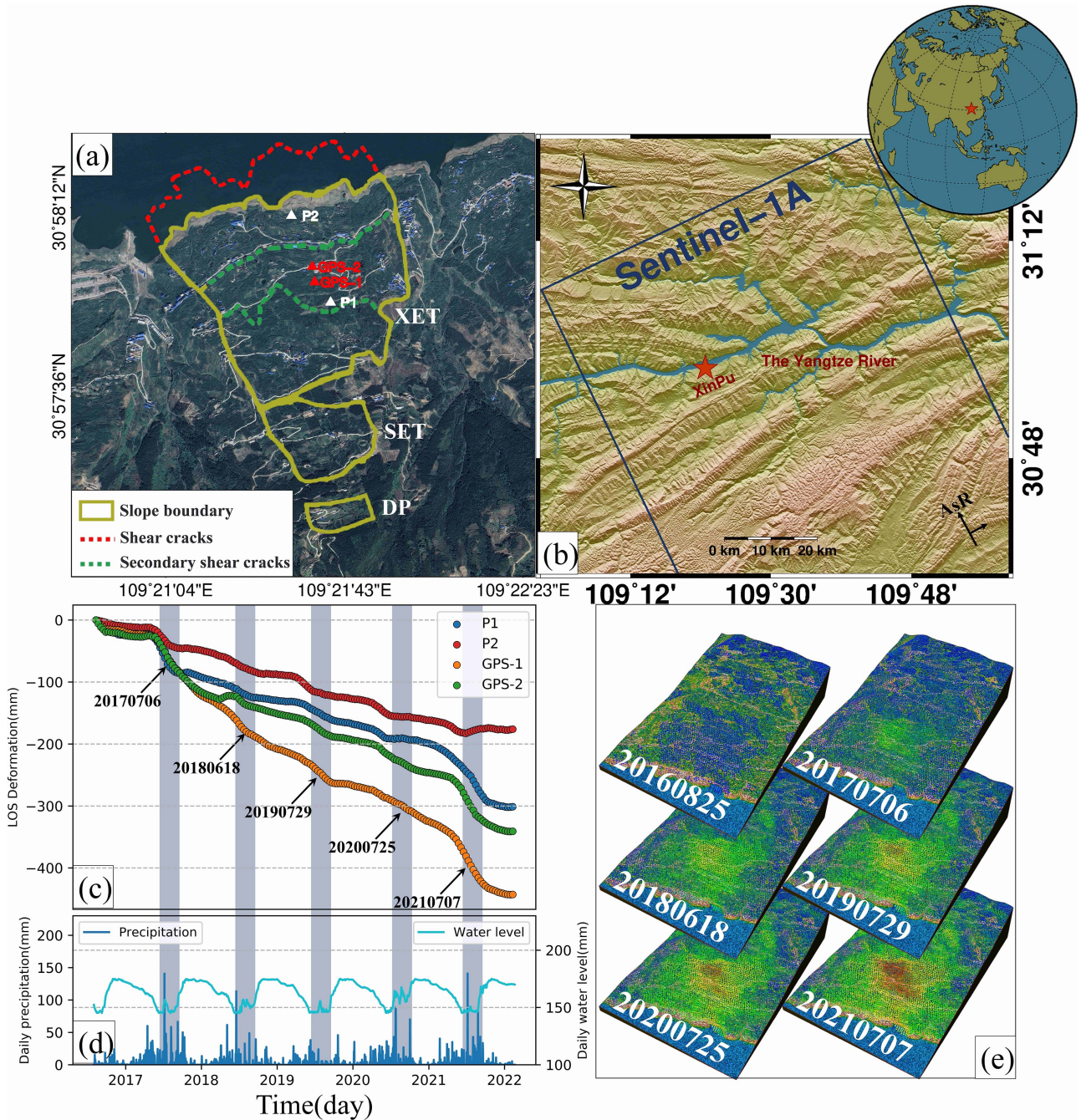


Fig. 3. (a) Optical image of Xinpu landslide and the slide boundary. Four points on the slope are selected for analysis. (b) Topographic map of the study area. Blue lines outline the coverage of the used Sentinel-1 data. (c) Time series deformation of the selected four points. (d) Reservoir water level and precipitation from 2016 to 2022. The heavy rainfall events on 6 July 2017, 18 June 2018, and 7 July 2021 are reflected in the deformation of the five points. The extraction and storage of the reservoir water level are also reflected in the deformation. (e) Time series deformation map.

The flood season in the study area takes place from June to July annually and is characterized by heavy rainfall. In preparation for the flood season, the reservoir water level is typically lowered through artificial discharge from early March. This discharge helps mitigate the risk of flooding, but also results in a reduction in the reservoir water level. The combination of artificial drainage and natural rainfall constitutes the primary factors contributing to landslide deformation during this period. It is worth noting that the leading edge of the Xiaertai (XET)

slope borders the Yangtze River valley [see Fig. 3(a)]. In this region, the occurrence of traction slip failure is attributed to the combined effects of precipitation and water level fluctuations. These factors, acting upon the XET slope, increase the likelihood of instability and contribute to the deformation of the slope during the flood season [36].

When the reservoir water level increases, it causes a rise in the groundwater level within the slope body. This rise in groundwater level leads to a decrease in the shear strength of the

TABLE I
SENTINEL-1 A TIME SERIES SAR DATA INFORMATION

Start Date(YYYY-MM-DD)	2016.08.01
End Date(YYYY-MM-DD)	2022.02.19
Number of Scenes	161
Revisit Period (days)	12
Orbit	Ascending
Track/Frame	84/95

slip zone due to the influence of pore pressure modulation caused by the higher reservoir water level. As a result, the stability of the slope is compromised, increasing the risk of deformation and landslides. Conversely, when the reservoir water level decreases, the downward dragging and unloading effect of the reservoir water on the landslide occur. This effect can accelerate the deformation of the slope, making it more susceptible to movement and instability. These changes in water level have a direct impact on the behavior of the slope, influencing its stability and deformation patterns [37]. The trailing edge of the XET slopes is positioned in the heart of the landslide, subject to frequent rainfall that washes over them. As a result, loose stones and soil blocks on the slope's surface are regularly displaced. These incessant erosion and displacement processes significantly contribute to the ongoing deformation of the slopes within this region of the landslide.

B. Data Analysis

We obtained 161 Sentinel-1 A images from 1 August 2016 to 19 February 2022 over Xinpu landslide. The cumulative deformation results of time series with a temporal resolution of 12 days were obtained using the ICA-assisted TCP-InSAR processing algorithm [38]. Additional SAR data information is provided in (Table I). In the data processing process, the data registration accuracy was guaranteed to reach 0.02 m, and the average coherence of the interference points was greater than 0.5. The RMS of the deformation point in a 200 m \times 200 m window far from the deformation area was calculated, and the results show that deformation monitoring accuracy was ensured to be better than 15 mm/year. Results show that XET landslide experienced significant slip from 2016 to 2022 [see Fig. 3(e)], which moved down the slope and reached -90 mm/year in the LOS direction. The displacement of the landslide center point reached 500 mm (LOS). The time-series cumulative deformation shows that the landslide deformation presented a periodic character, with larger displacement usually occurring in the summer, this phenomenon is because the landslide deformation is affected by seasonal rainfall or river level fluctuations. Daily frequency precipitation records were collected from NOAA for the period of 1st August 2016, to 19th February 2022. The precipitation measuring station (Station #57348) was located approximately 17 km away from the Xinpu landslide site.

The ground measurement data, GPS-1 and GPS-2, are situated in the central area of the XET landslide [see Fig. 3(a)]. These measurements correspond to the same period as the InSAR data and are updated daily, providing further validation for our methodology. P1 is located at the upper boundary of the landslide area, while P2 is positioned at the lower boundary [see Fig. 3(a)].

These points help us analyze the varying effects of rainfall and reservoir water level on deformation. During the flood season, which typically occurs from June to July, artificial water release is often conducted in early June to manage the increased water flow. This caused the water level of the reservoir to drop, which caused the landslide to move away from the satellite. This trend is observed at all four measurement points. Additionally, as heavy rainfall intensifies during the flood season, the displacement of the landslide surface increases. This phenomenon is particularly prominent at GPS-1, GPS-2, and P2 points located on the upper part of the landslide. However, it should be noted that after the 2021 summer rainstorm, the LOS deformation at P2 showed an elevated pattern. It is speculated that this phenomenon is caused by the accumulation of loose soil on the lower edge of the landslide. The rain washed away the loose soil on the upper edge of the landslide, causing it to fall toward the lower edge. Furthermore, in the summer of 2018, the water level in the reservoir remained stagnant for a certain period. During this time, deformation and uplift were observed at the GPS-2 point. Once the water level resumed falling, the deformation also decreased accordingly [see Fig. 3(c)].

C. Data Preparation

In the XET slope, we extracted 4905 Time-Coherent Points with a coherence value higher than 0.3 for EDSL. For each feature point, 1648 datasets were constructed, each consisting of three parts: 1) InSAR time series data and its time information (year, month and day); 2) rainfall time series data and time information (year, month, and day); and 3) reservoir water level and time information (year, month, and day). The length of each dataset needed to be adjusted for different scenarios. In Xinpu, when the accumulated rainfall reaches its peak, the landslide surface displacement increases rapidly. After analyzing the correlation between rainfall, reservoir water level and landslide surface displacement, we found that the landslide deformation lags behind rainfall and reservoir water level by approximately 10–22 days. Therefore, the lag coefficients of rainfall and reservoir water level (as described in Section II method) were set to a larger value (30) in this experiment. Fig. 3(c) shows that the periodicity of deformation is in years, so the deformation lag coefficient was also set to 30×12 days, encompassing the whole cycle of landslide deformation. All time-series data were divided into a 2:1 ratio, resulting in 1090 training sets and 558 test sets. The deformation data of the training set ranged from 1 August 2016 to 11 July 2020, while the test set spanned from 11 July 2020 to 19 February 2022.

IV. RESULTS

A. Validation of Deformation Estimation Results Using Ground Truth Measurements

There is interference from InSAR data processing errors in using ground GNSS monitoring data to evaluate the accuracy of HTF estimation results. Therefore, in order to accurately verify the accuracy of HTF estimation, we need to exclude the interference from InSAR data processing errors. For these two

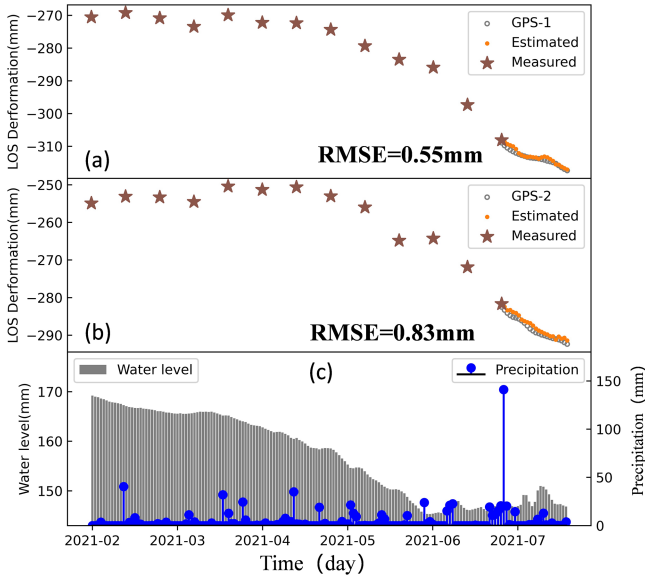


Fig. 4. Accuracy evaluation of HTF deformation estimation using ground truth measurements. (a) Performance of HTF deformation estimation at GPS-1. (b) Performance of HTF deformation estimation at GPS-2. (c) Reservoir water level and rainfall situation for the corresponding time period.

monitoring points, we calibrated the InSAR data using GNSS data to minimize the InSAR data processing errors, and then trained the model after this processing. We inputted the test data into the trained model to obtain HTF deformation estimation results from July 11, 2020 to February 19, 2022. These results were then compared with ground measured data collected from GPS-1 and GPS-2 points [see Fig. 4(a) and (b)]. During the period from March to June 2021, the reservoir continued to discharge water. It was observed that the corresponding InSAR measurements of land subsidence showed an accelerating trend during this period. On June 28, 2021, a heavy rainstorm occurred, accompanied by continuous rainfall before and after [see Fig. 4(c)]. However, in the month following June 28, 2021, neither GPS-1 nor GPS-2 exhibited significant immediate deformation, which is consistent with both estimates and ground measurements. Nevertheless, it is evident that the summer of 2021 received a significantly higher amount of rainfall compared to the previous summers of 2018–2020. As a result, the cumulative deformation in 2021 was the highest, indicating that while rainfall may not result in immediate deformation, long-term cumulative rainfall can contribute to future deformation acceleration. Therefore, relying solely on the traditional one-to-one mapping model method for estimating deformation is not entirely accurate. The RMSE between the estimated deformation value of GPS-1 and the ground measured value was calculated to be 0.55 mm. Similarly, for GPS-2, the RMSE between the estimated deformation value and the ground measurement was determined to be 0.83 mm.

B. Comparison of EDSL From Four Methods

To assess the effectiveness of MUSEnet's algorithm, we conducted three sets of controlled experiments using KF, KF-ARIMA, and KF-LSTM, respectively. Regarding overall estimation accuracy, the MUSEnet method achieved an RMSE as

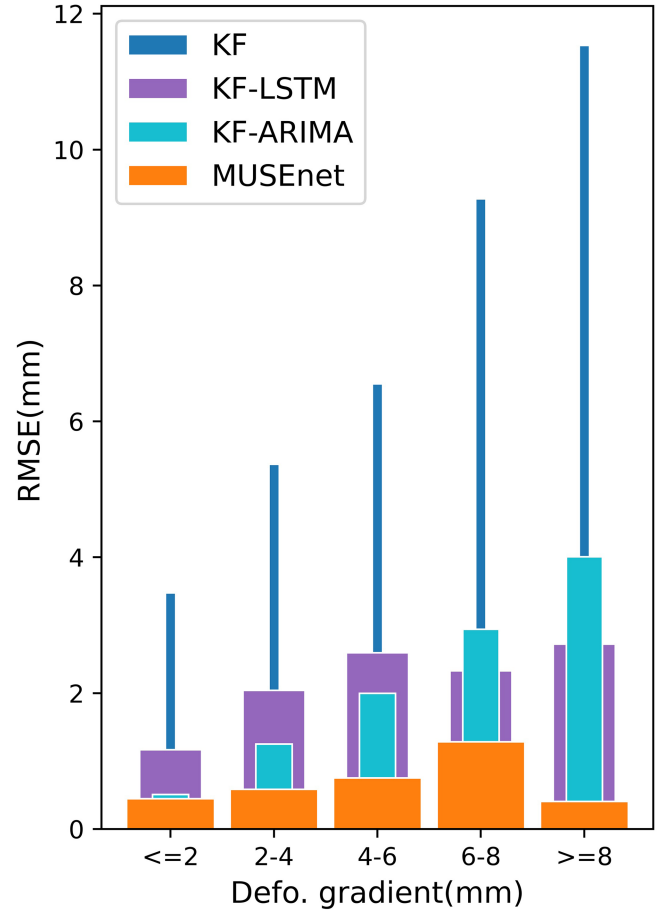


Fig. 5. Accuracy comparison of multiple methods.

low as 0.70 mm. It was followed by KF-ARIMA with 1.98 mm, KF-LSTM with 2.05 mm, and KF with the lowest accuracy level of 7.17 mm. In order to assess the method's estimation capability for varying magnitudes of deformation, we categorized the results into five groups based on the deformation gradient. We then evaluated the RMSE for each category (see Fig. 5). Among the five types of deformation gradients, KF exhibits the highest RMSE, indicating that its estimation accuracy is the lowest. Conversely, MUSEnet demonstrates the smallest RMSE among the five types of deformation gradients, suggesting the highest estimation accuracy. KF-LSTM and KF-ARIMA, supported by prediction models, exhibit some correction effects on the estimation results. As the absolute value of the deformation gradient increases, the estimation accuracy of model-driven KF-ARIMA and KF methods gradually decreases. However, the accuracy of data-driven KF-LSTM and MUSEnet does not exhibit this phenomenon. This suggests that the accuracy of data-driven methods is less influenced by the severity of deformation. In other words, data-driven methods demonstrate minimal susceptibility to error accumulation. This indicates that data-driven methods may have advantages over model-driven methods in terms of accuracy and robustness, particularly when dealing with severe deformations. Table II presents the values of four precision evaluation indexes (i.e., RMSE, MAE, MAPE, PC) at

TABLE II
ACCURACY EVALUATION

Defo.Gradient (mm)	Method	RMSE (mm)	MAE (mm)	MAPE (%)	PCC (%)
<2mm	KF	3.41	1.28	—	34.4
	KF-ARIMA	0.49	0.33	1.80	43.3
	MUSEnet	0.45	0.07	—	94.9
2-4mm	KF	5.33	2.60	3.54	46.1
	KF-ARIMA	1.18	0.94	1.04	73.4
	MUSEnet	0.58	0.10	0.06	98.9
4-6mm	KF	6.51	3.73	3.31	41.1
	KF-ARIMA	1.88	1.61	1.23	78.6
	MUSEnet	0.75	0.12	0.06	99.2
6-8mm	KF	9.23	5.87	2.15	33.3
	KF-ARIMA	2.72	2.27	0.95	77.4
	MUSEnet	1.28	0.21	0.07	98.9
>8mm	KF	11.37	8.12	2.61	31.1
	KF-ARIMA	3.62	2.96	1.03	73.8
	MUSEnet	0.40	0.14	0.05	99.3

The smaller RMSE, MAE and MAPE indicate the higher accuracy, while the larger PCC indicate the higher accuracy. The optimal result is shown in bold.

various deformation gradients. These values further elucidate the aforementioned issues.

Fig. 6(a) and (b) shows the test results of EDSL at GPS-1 and GPS-2 points, respectively. The upper and middle rows of Fig. 6(c)–(h) display the EDSL details of individual test results at GPS-1 and GPS-2 points, respectively, while the lower panel displays the corresponding hydrological data, including precipitation and reservoir water level. This figure provides a concise and informative visual representation that demonstrates the EDSL estimation results and the observed hydrological data in the study. In Fig. 6(b) and (c), the estimation effect of small deformation is depicted, where the deformation gradient (the instantaneous gradient between two SAR scenes) is less than 2 mm. Fig. 6(d) and (e) illustrates the estimation effect of moderate deformation, with gradients greater than 4 mm and less than 6 mm. Finally, Fig. 6(f) and (g) depicts the estimation effect of large deformation, where the deformation gradients are greater than 8 mm. According to the order of deformation gradient from small to large, the accuracy of MUSEnet improves by 13%, 58%, 67%, 73%, and 91% compared to the other optimal method. Particularly, the maximum deformation of XET occurs from May to September each year, and the displacement exceeds 8 mm per day during this period. In this case, MUSEnet is able to provide an average accuracy estimation of 0.14 mm, while KF-ARIMA is only able to provide a estimation accuracy of 2.96 mm.

Upon careful comparison, we have discovered that both the KF method and the KF-based method require a quantitative relationship between precipitation, reservoir level, and landslide deformation obtained from previous studies. However, in our specific study area, this relationship proves to be inapplicable. Consequently, it is not feasible to utilize hydrological factors to accurately simulate renewed measurements of landslide deformation. Furthermore, it is essential to note that these methods do not incorporate the hysteresis effects of deformation or the combined impacts of historical deformation. As a consequence, the estimates generated by these methods are prone to being unreliable.

C. Evaluation of Estimation Performance Under Two Hydrological Phenomena

To further demonstrate the effectiveness of MUSEnet, we conducted an analysis encompassing two hydrological phenomena: two instances of extreme rainfall events and two fluctuations in the reservoir water level. Study have indicated that the slope ridge point at the top of the slope is particularly susceptible to intense rainfall events, while the slope foot point near the reservoir bank is highly vulnerable to variations in the reservoir water level [39]. With this in mind, we employed point P1 [see Fig. 3(a)] to evaluate the estimation performance of HTF deformations during extreme rainstorms, as shown in Fig. 7(b)–(e) and (g)–(j), while point P2 [see Fig. 3(a)] was utilized to assess the estimation performance of HTF deformations during reservoir water level fluctuations, as shown in Fig. 8(b)–(k) and (g)–(j).

The initial heavy rainfall event took place on July 28, 2020 [see Fig. 7(f)]. However, based on the InSAR measurements of the instantaneous rate, it was observed that this heavy rainfall event did not immediately trigger any deformation. Instead, its impact was observed during several days of continuous light rainfall around August 6 [see Fig. 7(f)]. Notably, MUSEnet's estimated results align with the InSAR measurements in terms of the observed deformation patterns [Fig. 7(e)]. Conversely, both the KF results and the derived method of KF indicate a sudden increase in the deformation rate on July 28, which contradicts the actual situation [Fig. 7(b), (c), and (d)]. Similarly, the second heavy rainfall event took place on July 8, 2021 [see Fig. 7(k)]. However, once again, InSAR measurements and the corresponding instantaneous rate did not show immediate deformation triggered by this rainfall event [see Fig. 7(k)]. Nonetheless, it is evident that the overall deformation rate during the summer of 2021 is greater than that observed during the summer of 2020 [see Fig. 7(f) and (k)]. The results obtained from MUSEnet provide an explanation for this phenomenon [see Fig. 7(j)]. However, it is worth noting that the results obtained from the KF and its derived methods still display significant magnitudes of deformation on July 8 (Fig. 7(g), (h), and (i)). Furthermore, the application of the KF method leads to subsequent error propagation [see Fig. 7(g)]. The evaluation of the estimation effect for the two heavy precipitation events demonstrates that the traditional one-to-one mapping estimation model is not appropriate. In contrast, MUSEnet proves to be a more advanced and sophisticated method for accurately estimating the deformation caused by these events.

In March 2021, the reservoir initiated a gradual water release. Subsequently, the water level in the reservoir experienced a rapid decline from May to June. From June to August, the water level remained consistently at its lowest point without significant fluctuations [see Fig. 8(f)]. During the period from May to June, the InSAR deformation rate remained stable at -0.3 mm/day. However, there was almost no deformation observed from June to August, with the deformation rate during this period being approximately 0 [see Fig. 8(f)]. Importantly, the deformation rate estimated by MUSEnet aligns closely with the measurements obtained through InSAR monitoring [see Fig. 8(e)]. On the

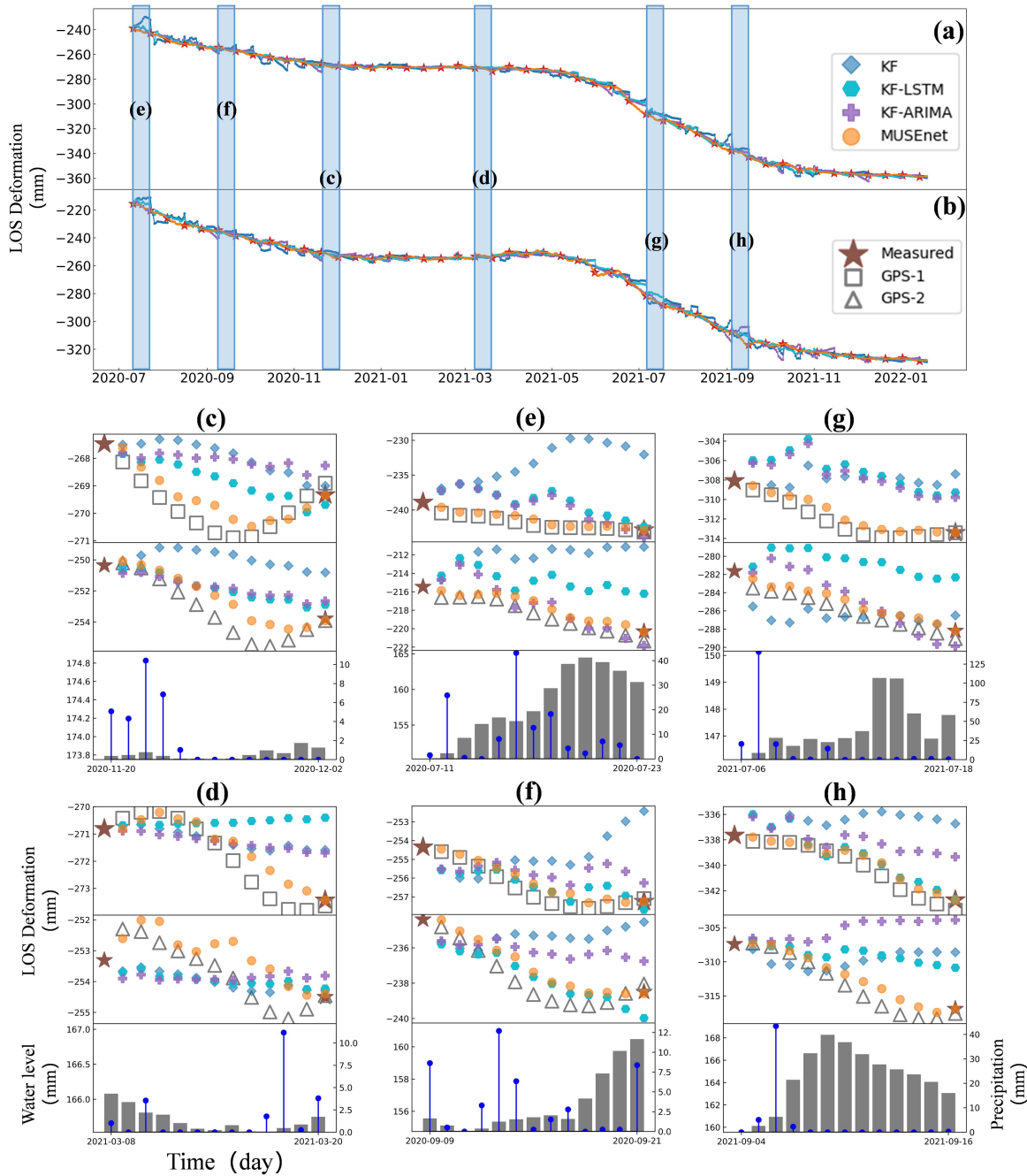


Fig. 6. (a), (b) EDSL results at GPS-1 and GPS-2. (c), (d) Gradient of deformation is less than 2 mm. (e), (f) Gradient of deformation is greater than 2 mm and less than 4 mm. (g), (h) Gradient of deformation is greater than 8 mm.

other hand, the estimation results of alternative methods failed to reveal any correlation between deformation and the reservoir water level. However, a notable discrepancy emerged on July 8, 2021, which could potentially be attributed to the influence of rainfall data [see Fig. 8(b), (c), and (d)]. In late August, the reservoir water level started to recover, and the deformation near the reservoir bank moved along the LOS direction toward the satellite direction. This deformation remained stable following the rise in the reservoir water level [see Fig. 8(k)]. Regarding the estimation results obtained from the KF and its derivative

methods, they showed significant noise. These methods failed to observe a clear correlation between the reservoir water level and the deformation [see Fig. 8(g), (h), and (i)]. It is possible that the presence of rainfall data may have affected these estimation results. The evaluation of the estimation effect of reservoir water level release and storage events reveals that the traditional model is highly vulnerable to the influence of rainfall events. This observation further highlights that in traditional methods, incorrect weight allocation between rainfall and reservoir level data can result in estimation errors.

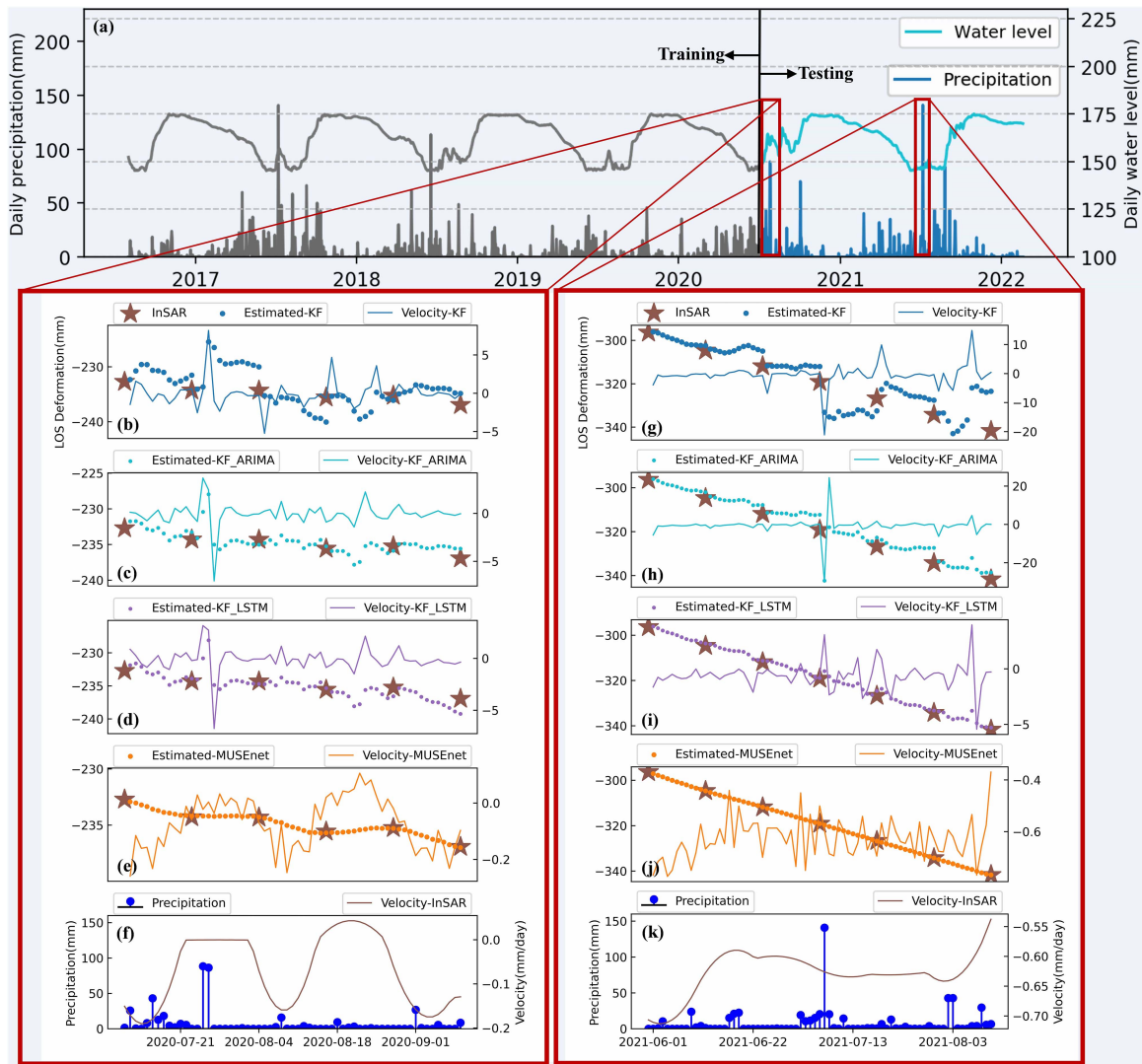


Fig. 7. Performance of four methods in two heavy rainfall events. (a) Rainfall and reservoir water level maps for the full time period. (b)–(e) and (g)–(j) HTF estimation results and instantaneous deformation rates of four methods. (f) and (k) Rainfall amount and instantaneous deformation rate of InSAR displacement for the corresponding time period.

V. DISCUSSION

The landslides occurring in the Yangtze River basin are influenced by rainfall and reservoir water levels. During rainfall events, loose rocks and soils on the slope may dislodge, leading to deformation that typically occurs along the ridge of the slope. On the other hand, fluctuations in the reservoir water level can cause displacement of the landslide due to changes in pore water pressure and the dragging effect of water, resulting in deformation primarily distributed at the foot of the slope. However, accurately assigning weight factors using traditional methods is challenging, and this can hinder the effective utilization of rainfall and reservoir water level data in deformation estimation. To explore the potential improvement in estimation performance of slope foot and ridge deformation using MUSEnet and hydrological data, as well as the automatic optimization of weight allocation for multiple hydrological factors, we conducted a correlation analysis between Xinpu XET landslide deformation

and rainfall, as well as reservoir water level. By selecting feature points P1 and P2 located at the ridge and foot of the slope, respectively [see Fig. 3(a)], we evaluated MUSEnet’s estimation performance by applying different hydrological factors individually and in combination.

To assess the correlation and independence between reservoir water level, rainfall, and surface deformation, we employed a chi-square test. This test assumes independence between hydrological observations and deformation, with a predefined significance level of 0.05. The results of the squareroot test indicated that 82.6% of the monitoring points did not align with the hypothesis of independence between reservoir water level and surface deformation. In addition, for 93.5% of the monitoring points, the P-value was lower than the significance level, suggesting that rainfall and surface deformation are not independent. These findings indicate a high correlation between reservoir water level, rainfall, and Xinpu landslide deformation. We identified specific points on the landslide surface that exhibit

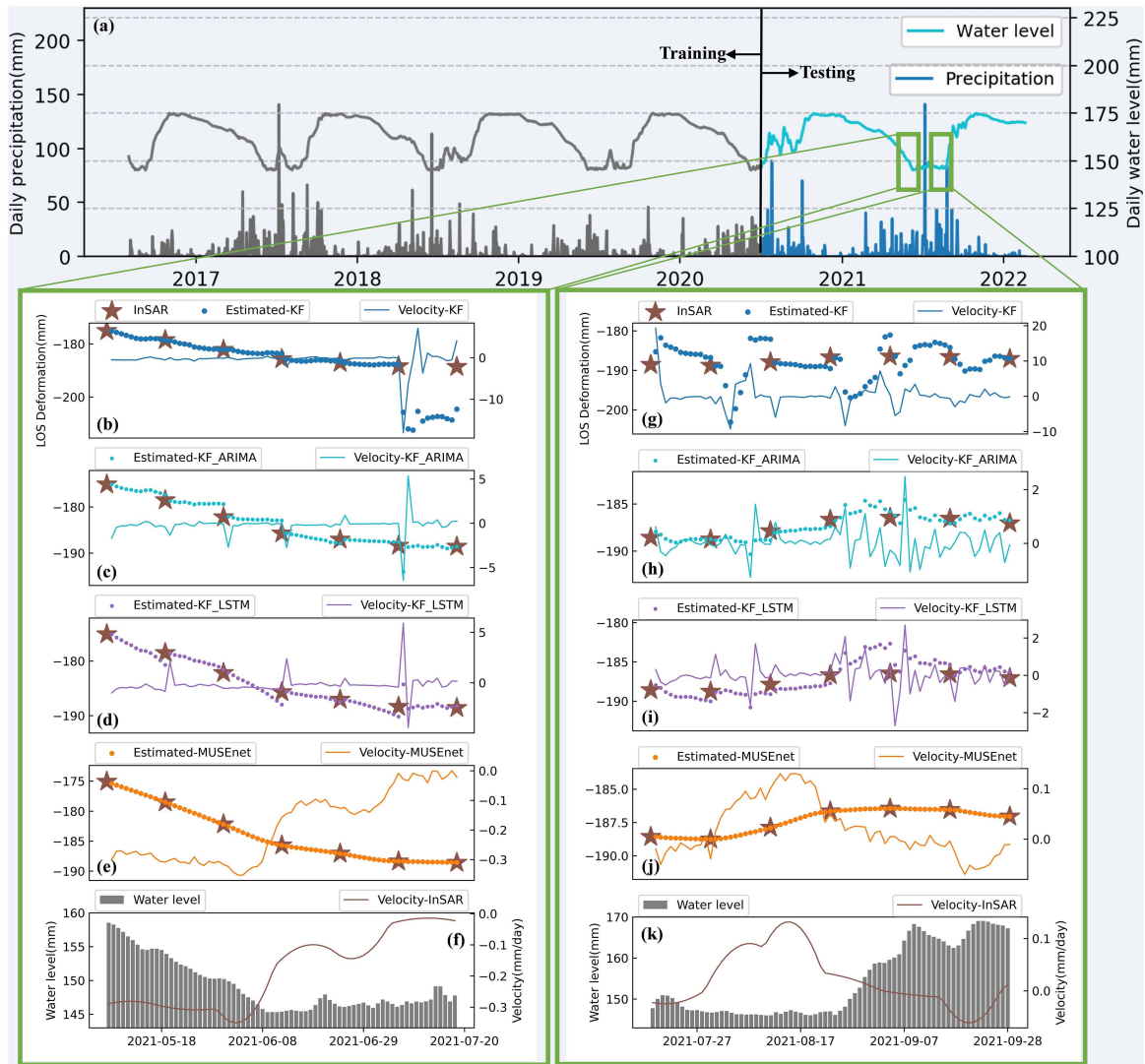


Fig. 8. Performance of four methods in reservoir water level fluctuations. (a) Rainfall and reservoir water level maps for the full time period. (b)–(e) and (g)–(j) HTF estimation results and instantaneous deformation rates of four methods. (f) and (k) Reservoir water level and instantaneous deformation rate of InSAR displacement for the corresponding time period.

a correlation between hydrological observations and surface deformation. The Chi-square statistic was subsequently normalized to consider the degree of correlation across various regions. Within the entire landslide area, we observed that the correlation between rainfall and slope top deformation is the strongest [see Fig. 9(a)]. Similarly, the correlation between reservoir water level and slope foot deformation is also the highest [see Fig. 9(b)].

The impact factors of the three datasets are precipitation (IFP, circle), reservoir water level (IFW, square), and precipitation and reservoir water level (IFPW, triangle), respectively. The basic information of the datasets are described as follows.

1) *Dataset S1 (IFP)*: The dataset has 1090 groups of data, each group of data consists of 30 historical precipitation and 30 InSAR historical deformation and their year, month, and day, the dimension of the dataset is [1090, 60, 4].

2) *Dataset S2 (IFW)*: The dataset has 1090 groups of data, each group of data consists of 30 historical reservoir water level

and 30 InSAR historical deformation and their year, month, and day, the dimension of the dataset is [1090, 60, 4].

3) *Dataset S3 (IFPW)*: The dataset has 1090 groups of data, each group of data consists of 30 historical precipitation, 30 historical reservoir water level, and 30 InSAR historical deformation and their year, month, and day, the dimension of the dataset is [1090, 90, 4].

Based on the results of the KF and KF-derived methods, it has been observed that at location P1 [Fig. 3(a)], the RMSE of the IFP is smaller compared to the IFW [Fig. 10(a), (b), and (c)]. This implies that the influence of rainfall on deformation estimation is greater than that of the reservoir water level at P1. The reason behind this observation is that P1 is situated on a ridge, where deformation is primarily caused by rain erosion and is less impacted by the fluctuations in the reservoir water level. On the other hand, P2 is located at the foot of the mountain [see Fig. 3(a)], where the deformation is mainly affected by the rise and fall of the reservoir water level, and is less influenced

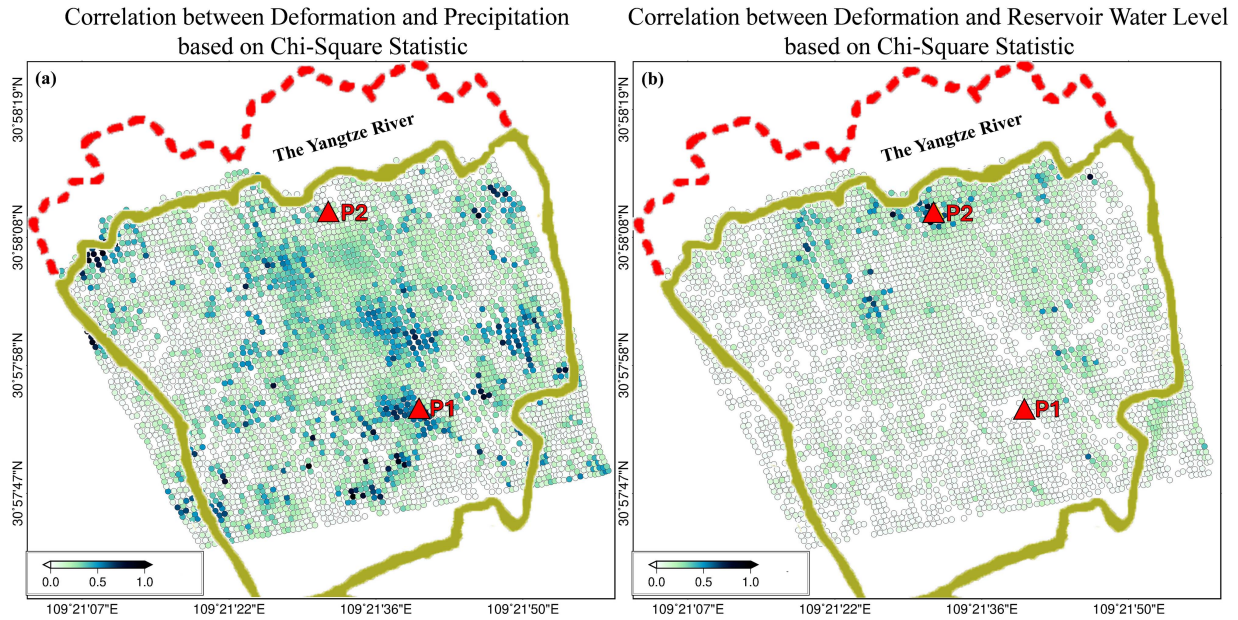


Fig. 9. Correlation analysis between hydrological observations and surface deformation based on chi-square statistics.

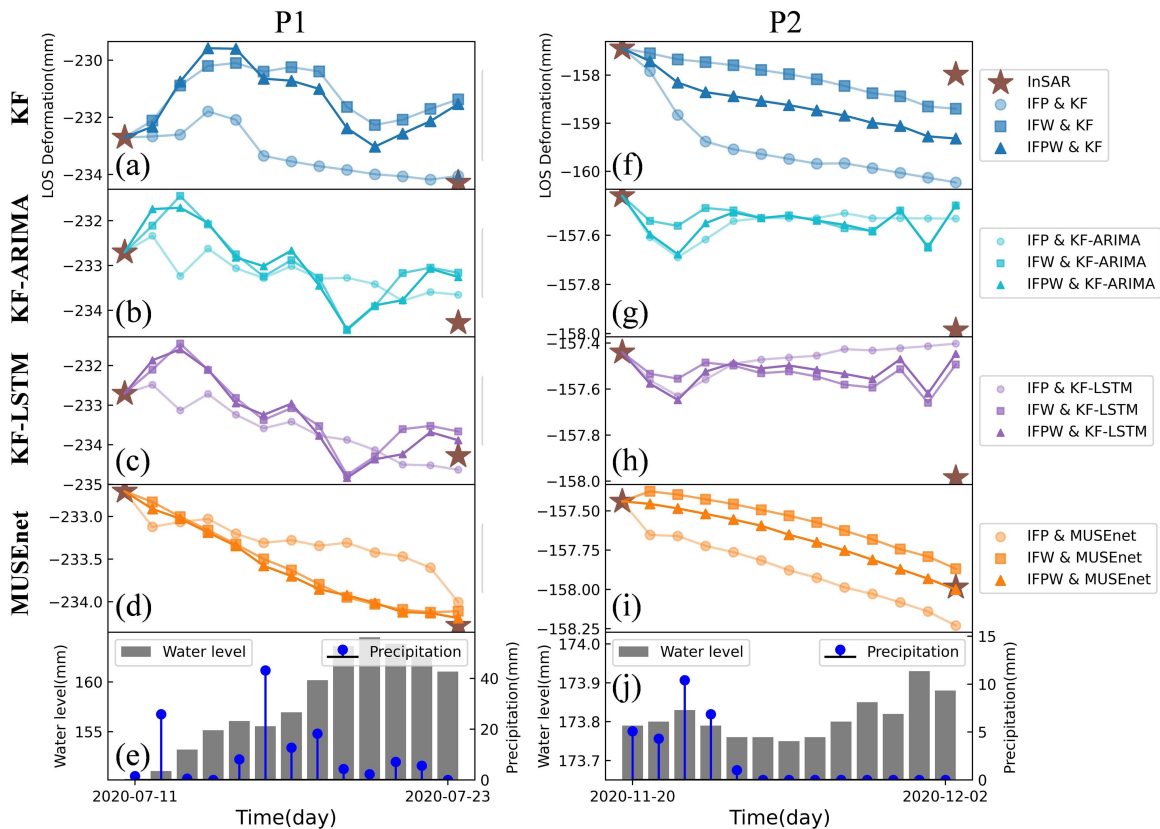


Fig. 10. Comparison of estimation effects at the ridge point P1 and the foot point P2. Combining IFP, IFW, and IFPW datasets with four estimation methods: Analysis of 12 estimation results.

by rainfall. Consequently, the RMSE of the IFW is smaller than that of the IFP due to the stronger auxiliary effect of the reservoir water level data on estimating the deformation at P2 [see Fig. 10(f), (g), and (h)]. In the collaborative prediction of reservoir water level and rainfall, it is observed that the

prediction accuracy can be reduced when incorporating data with low correlation. On the other hand, the estimation accuracy of MUSEnet, a specific method, is improved when supported by both hydrological observations. This improvement suggests that MUSEnet has the capability to intelligently adjust the weights of

the two hydrological observations, resulting in higher accuracy predictions.

By taking into account multiple sources of data, such as reservoir water level and rainfall, MUSEnet can effectively leverage their combined information to enhance the accuracy of predictions. The intelligent adjustment of weights allows MUSEnet to assign higher importance or influence to the hydrological observations that contribute more significantly to the prediction task, while de-emphasizing or disregarding less relevant or poorly correlated data. This ability to adaptively assign weights based on the data's importance or correlation enables MUSEnet to achieve improved estimation accuracy compared to other methods that do not possess this capability.

VI. CONCLUSION

InSAR technology has been widely used as an effective monitoring method for landslide deformation. However, the deformation derived from InSAR is not considered to be the main data source for landslide hazard warning. This limitation comes from the temporal resolution of InSAR-derived deformation, which is usually between 11 and 24 days and does not meet the requirements of early warning. To solve this problem, we propose a deep learning framework that uses InSAR data for daily deformation estimation. Our framework combines HTF hydrological observations to improve the accuracy and temporal resolution of deformation estimates. This algorithm is used to estimate the landslide deformation of Xinpu landslide in the Three Gorges Reservoir area of China in daily terms. The resulting time series deformation shows that there is no simple one-to-one correspondence between hydrological observation and landslide deformation. Our study can use hydrological observations to more accurately predict the HTF deformation of reservoir landslides. This method provides a cost-effective way to provide a detailed deformation field before a landslide disaster occurs, thus helping to protect the lives and property of local residents.

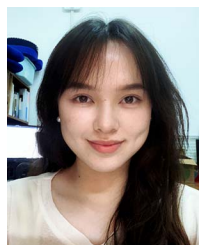
ACKNOWLEDGMENT

The authors would like to thank the Generic Mapping Tools (GMT) software for providing the mapping platform. Sentinel-1 images were provided by the Alaska Satellite Press (download url: <https://asf.alaska.edu/data-sets/sar-data-sets/sentinel-1/>). Rainfall data were provided by the China Meteorological Administration (download url: <https://www.ncei.noaa.gov/access/search/data-search/global-summary-of-the-day/>).

REFERENCES

- [1] K. Dai et al., "Dynamic landslides susceptibility evaluation in Baihetan dam area during extensive impoundment by integrating geological model and inSAR observations," *J. Appl. Earth Observ. Geoinf.*, vol. 116, 2023, Art. no. 103157.
- [2] B. Huang, Y. Yin, and C. Du, "Risk management study on impulse waves generated by Hongyanzi landslide in three Gorges reservoir of China on Jun. 24, 2015," *Landslides*, vol. 13, no. 3, pp. 603–616, 2016.
- [3] Y. Liu, X. Wang, Z. Wu, Z. He, and Q. Yang, "Simulation of landslide-induced surges and analysis of impact on dam based on stability evaluation of reservoir bank slope," *Landslides*, vol. 15, no. 10, pp. 2031–2045, 2018.
- [4] Q. Lei, D. Sornette, H. Yang, and S. Loew, "Real-time forecast of catastrophic landslides via Dragon-King detection," *Geophys. Res. Lett.*, vol. 50, no. 6, 2023, Art. no. e2022GL100832.
- [5] P. Liu et al., "Using advanced inSAR time series techniques to monitor landslide movements in Badong of the three Gorges region, China," *Int. J. Appl. Earth Observ. Geoinf.*, vol. 21, pp. 253–264, 2013.
- [6] Q. Sun, L. Zhang, X. L. Ding, J. Hu, Z. W. Li, and J. J. Zhu, "Slope deformation prior to Zhouqu, China landslide from inSAR time series analysis," *Remote Sens. Environ.*, vol. 156, pp. 45–57, 2015.
- [7] J. Zhu, Z. Li, and J. Hu, "Research progress and methods of inSAR for deformation monitoring," *Acta Geodaetica et Cartographica Sinica*, vol. 46, no. 10, 2017, Art. no. 1717.
- [8] N. Cenni, S. Fiaschi, and M. Fabris, "Integrated use of archival aerial photogrammetry, GNSS, and inSAR data for the monitoring of the Patigno landslide (Northern Apennines, Italy)," *Landslides*, vol. 18, pp. 2247–2263, 2021.
- [9] R. Bonì, M. Bordoni, A. Colombo, L. Lanteri, and C. Meisina, "Landslide state of activity maps by combining multi-temporal A-DinSAR (LAMBDA)," *Remote Sens. Environ.*, vol. 217, pp. 172–190, 2018.
- [10] A. van Natijne, T. Bogaard, F. van Leijen, R. Hanssen, and R. Lindenbergh, "World-wide inSAR sensitivity index for landslide deformation tracking," *Int. J. Appl. Earth Observ. Geoinf.*, vol. 111, 2022, Art. no. 102829.
- [11] X. Hu, Z. Lu, T. C. Pierson, R. Kramer, and D. L. George, "Combining inSAR and GPS to determine transient movement and thickness of a seasonally active low-gradient translational landslide," *Geophysical Res. Lett.*, vol. 45, no. 3, pp. 1453–1462, 2018.
- [12] J. Zhou et al., "Research and prospect on disaster-causing mechanism and prevention-control technology of reservoir landslides," *Adv. Eng. Sci.*, vol. 55, no. 1, pp. 110–128, 2023.
- [13] S. Moretto, F. Bozzano, C. Esposito, P. Mazzanti, and A. Rocca, "Assessment of landslide pre-failure monitoring and forecasting using satellite SAR interferometry," *Geosciences*, vol. 7, no. 2, 2017, Art. no. 36.
- [14] L. Wang, Z. Zhang, B. Huang, M. Hu, and C. Zhang, "Triggering mechanism and possible evolution process of the ancient Qingshi landslide in the three Gorges reservoir," *Geomatics, Natural Hazards Risk*, vol. 12, no. 1, pp. 3160–3174, 2021.
- [15] J. Cohen-Waeber, R. Bürgmann, E. Chaussard, C. Giannico, and A. Ferretti, "Spatiotemporal patterns of precipitation-modulated landslide deformation from independent component analysis of inSAR time series," *Geophysical Res. Lett.*, vol. 45, pp. 1878–1887, 2018.
- [16] R. Tomas, Z. Li, J. M. Lopez-Sanchez, P. Liu, and A. Singleton, "Using wavelet tools to analyse seasonal variations from inSAR time-series data: A case study of the Huangtupo landslide," *Landslides*, vol. 13, no. 3, pp. 437–450, 2016.
- [17] L. Piciullo, M. Calvello, and J. Cepeda, "Territorial early warning systems for rainfall-induced landslides," *Earth-Sci. Rev.*, vol. 179, pp. 228–247, 2018.
- [18] Q. Xu et al., "Successful implementations of a real-time and intelligent early warning system for loess landslides on the Heifangtai Terrace, China," *Eng. Geol.*, vol. 278, 2020, Art. no. 105817.
- [19] J. Cai et al., "A new algorithm for landslide dynamic monitoring with high temporal resolution by Kalman filter integration of multiplatform time-series inSAR processing," *Int. J. Appl. Earth Observ. Geoinf.*, vol. 110, 2022, Art. no. 102812.
- [20] X. Shi, J. Wang, M. Jiang, S. Zhang, Y. Wu, and Y. Zhong, "Extreme rainfall-related accelerations in landslides in Danba county, Sichuan province, as detected by inSAR," *Int. J. Appl. Earth Observ. Geoinf.*, vol. 115, 2022, Art. no. 103109.
- [21] B. Bayer, A. Simoni, M. Mulas, A. Corsini, and D. Schmidt, "Deformation responses of slow moving landslides to seasonal rainfall in the Northern Apennines, measured by inSAR," *Geomorphology*, vol. 308, pp. 293–306, 2018.
- [22] V. Tsironi, A. Ganas, I. Karamitros, E. Efstathiou, I. Koukouvelas, and E. Sokos, "Kinematics of active landslides in Achaia (Peloponnese, Greece) through inSAR time series analysis and relation to rainfall patterns," *Remote Sens.*, vol. 14, 2022, Art. no. 844.
- [23] C. Zhao, Z. Lu, Q. Zhang, and J. de la Fuente, "Large-area landslide detection and monitoring with ALOS/PALSAR imagery data over Northern California and Southern Oregon, USA," *Remote Sens. Environ.*, vol. 124, pp. 348–359, 2012.
- [24] L. Qinghao, Z. Yonghong, D. Min, W. Hongan, K. Yonghui, and W. Jujie, "Time series prediction method of large-scale surface subsidence based on deep learning," *Acta Geodaetica et Cartographica Sinica*, vol. 50, no. 3, 2021, Art. no. 396.

- [25] X. Z. Li and J. M. Kong, "Application of GA-SVM method with parameter optimization for landslide development prediction," *Natural Hazards Earth Syst. Sci.*, vol. 14, no. 3, pp. 525–533, 2014.
- [26] P. Hill, J. Biggs, V. Ponce-López, and D. Bull, "Time-series prediction approaches to forecasting deformation in Sentinel-1 inSAR data," *J. Geophysical Res., Solid Earth*, vol. 126, no. 3, 2021, Art. no. e2020JB020176.
- [27] M. Dalaison and R. Jolivet, "A Kalman filter time series analysis method for inSAR," *J. Geophysical Res., Solid Earth*, vol. 125, no. 7, 2020, Art. no. e2019JB019150.
- [28] A. L. Handwerger, E. J. Fielding, S. S. Sangha, and D. P. S. Bekaert, "Landslide sensitivity and response to precipitation changes in wet and dry climates," *Geophysical Res. Lett.*, vol. 49, no. 13, 2022, Art. no. e2022GL099499, doi: [10.1029/2022gl099499](https://doi.org/10.1029/2022gl099499).
- [29] J. Liu, F. Rahmani, K. Lawson, and C. Shen, "A multiscale deep learning model for soil moisture integrating satellite and in situ data," *Geophysical Res. Lett.*, vol. 49, no. 7, 2022, Art. no. e2021GL096847, doi: [10.1029/2021gl096847](https://doi.org/10.1029/2021gl096847).
- [30] F. A. Gers, J. Schmidhuber, and F. Cummins, "Learning to forget: Continual prediction with LSTM," *Neural Computation*, vol. 12, no. 10, pp. 2451–2471, 2000.
- [31] S. V. Gade, P. Sreenivas, S. A. Rao, A. Srivastava, and M. Pradhan, "Impact of the ensemble Kalman filter based coupled data assimilation system on seasonal prediction of Indian summer monsoon rainfall," *Geophysical Res. Lett.*, vol. 49, 2022, Art. no. e2021GL097184.
- [32] N. J. Finnegan, E. E. Brodsky, H. M. Savage, A. L. Nereson, and C. R. Murphy, "Seasonal slow landslide displacement is accommodated by mm-scale stick-slip events," *Geophysical Res. Lett.*, vol. 49, no. 20, 2022, Art. no. e2022GL099548, doi: [10.1029/2022gl099548](https://doi.org/10.1029/2022gl099548).
- [33] S. Pan, W. Gao, and R. Hu, "Physical modeling for large-scale landslide with chair-shaped bedrock surfaces under precipitation and reservoir water fluctuation conditions," *Water*, vol. 14, no. 6, 2022, Art. no. 984.
- [34] M. Xia, G. M. Ren, S. S. Zhu, and X. L. Ma, "Relationship between landslide stability and reservoir water level variation," *Bull. Eng. Geol. Environ.*, vol. 74, no. 3, pp. 909–917, 2014.
- [35] X. Yi et al., "The initial impoundment of the Baihetan reservoir region (China) exacerbated the deformation of the Wangjiashan landslide: Characteristics and mechanism," *Landslides*, vol. 19, no. 8, pp. 1897–1912, 2022.
- [36] G. Aoqing et al., "N-beats deep learning method for landslide deformation monitoring and prediction based on inSAR: A case study of Xinpu landslide," *Acta Geodaetica et Cartographica Sinica*, vol. 51, no. 10, 2022, Art. no. 2171.
- [37] G. Huang, J. Wang, Y. Du, Z. Bai, and D. Wang, "Time-delay analysis and prediction of landslide considering precipitation and reservoir water level—A case study of Xinpu landslide in three Gorges Reservoir Area, China," *J. Earth Sci. Environ.*, vol. 15, no. 3, pp. 621–631, 2021.
- [38] L. Zhang, X. Ding, and Z. Lu, "Ground settlement monitoring based on temporarily coherent points between two SAR acquisitions," *ISPRS J. Photogrammetry Remote Sens.*, vol. 66, no. 1, pp. 146–152, 2011.
- [39] W. Zheng et al., "Enhanced kinematic inversion of 3-D displacements, geometry, and hydraulic properties of a north-south slow-moving landslide in three Gorges Reservoir," *J. Geophysical Res.: Solid Earth*, vol. 128, no. 6, 2023, Art. no. e2022JB026232.



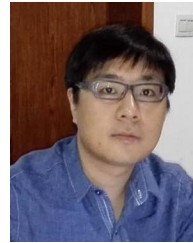
Aoqing Guo received the bachelor's degree in geodesy and surveying engineering from Central South University, Hunan, China, in 2021. She is currently working toward the Ph.D. degree with the Department of Surveying and Mapping Science and Technology, Central South University, Changsha, China.

She is highly interested in deep learning, data processing of InSAR technology, landslide deformation monitoring, and prediction.



Qian Sun received the M.Eng. and Ph.D. degrees in geodesy and surveying engineering from Central South University, Changsha, China, in 2008 and 2015, respectively.

She is currently a Associate Professor with the School of Geographical Sciences, College of Geographic Science, Hunan Normal University. She is the author of more than 20 articles in international peer-reviewed journals. Her research interests include geological hazard monitoring and interpretation based on radar satellite remote sensing.



Jun Hu (Senior Member, IEEE) received the M.Eng. and Ph.D. degrees in geodesy and surveying engineering from Central South University, Changsha, China, in 2008 and 2013, respectively.

From 2013 to 2014, he was a Postdoctoral Fellow with the Department of Land Surveying and GeoInformatics, The Hong Kong Polytechnic University, Hong Kong. He is currently a Full Professor with the Department of Geomatics and Remote Sensing, School of Geosciences and Info-Physics, Central South University. He is the author of more than 60

articles in international peer-reviewed journals. His research interests include mapping multidimensional and high-precision deformations under complicated environment and its applications in geophysical fields.



Wanji Zheng received the bachelor's and master's degrees in geodesy and surveying engineering from the School of Geosciences and Info-Physics, Central South University, Changsha, China, in 2015 and 2018, respectively, where he is currently working toward the Ph.D degree in geodesy.

His research interests include interferometric synthetic aperture radar and its applications on multidimensional landslide movements mapping.



Rong Gui received the M.E. and Ph.D. degrees in signal and information processing from Wuhan University, Wuhan, China, in 2016 and 2021, respectively.

She is currently working as a Lecturer with the Department of Geomatics and Remote Sensing, School of Geosciences and Info-Physics, Central South University, Changsha, China. Her research interests include synthetic aperture radar (SAR) imagery processing, multisource fusion algorithms of SAR, 3-D laser measurement technology, and pattern recognition.



Yana Yu received the B.S. degree in geographic information science from the China university of Mining and Technology, Xuzhou, China, in 2020, and the M.E. degree in geodesy and surveying engineering from Central South University, Changsha, China, in 2023.

Her research interests include polarimetric SAR classification and spatial distribution of landslides deformations.